nature geoscience

Article

https://doi.org/10.1038/s41561-025-01709-0

Observational constraints imply limited future Atlantic meridional overturning circulation weakening

Received: 21 May 2024

Accepted: 25 April 2025

David B. Bonan [1,6,7] ✉, **Andrew F. Thompson** [1], **Tapio Schneider** [1], **Laure Zanna** [2], **Kyle C. Armour** [3,4] **& Shantong Sun** [5]

The degree to which the Atlantic meridional overturning circulation (AMOC) weakens over the twenty-first century varies widely across climate models, with some predicting substantial weakening. Here we show that this uncertainty can be greatly reduced by using a thermal-wind expression that relates the AMOC strength to the meridional density difference and the overturning depth in the Atlantic. This expression captures the intermodel spread in AMOC weakening, with most of the spread arising from overturning depth changes. The overturning depth also establishes a crucial link between the present-day and future AMOC strength. Climate models with a stronger and deeper present-day overturning tend to predict larger weakening and shoaling under warming because the present-day North Atlantic is less stratified, allowing for a deeper penetration of surface buoyancy flux changes, larger density changes at depth and, consequently, larger AMOC weakening. By incorporating observational constraints, we conclude that the AMOC will experience limited weakening of about 3–6 Sv (about 18–43%) by the end of this century, regardless of emissions scenario. These results indicate that the uncertainty in twenty-first-century AMOC weakening and the propensity to predict substantial AMOC weakening can be attributed primarily to climate model biases in accurately simulating the present-day ocean stratification.

State-of-the-art global climate models (GCMs) consistently predict that the Atlantic meridional overturning circulation (AMOC) will weaken in response to rising greenhouse gas concentrations over the twenty-first century[1–4]. This weakening is important because the AMOC plays a crucial role in ventilating the upper 2,000 m of the ocean[5] and transporting heat northwards throughout the Atlantic Ocean[6]. These processes regulate Atlantic sea surface temperatures, which have wide-ranging impacts on regional climates over North America and Western Europe[7,8], Arctic sea-ice variability[9,10] and the location of tropical precipitation[11–13]. Moreover, changes in the AMOC strength are expected to strongly influence regional sea-level rise[14–16] and regional climate change[17–19] over the twenty-first century.

While GCMs consistently predict twenty-first-century AMOC weakening, the rate and magnitude of this weakening varies widely across GCMs, adding considerable uncertainty to future climate projections. For example, GCMs participating in Phase 6 of the Coupled Model

---

[1]Environmental Science and Engineering, California Institute of Technology, Pasadena, CA, USA. [2]Courant Institute of Mathematical Sciences, New York University, New York City, NY, USA. [3]Department of Atmospheric and Climate Science, University of Washington, Seattle, WA, USA. [4]School of Oceanography, University of Washington, Seattle, WA, USA. [5]Laoshan Laboratory, Qingdao, China. [6]Present address: Department of Atmospheric and Climate Science, University of Washington, Seattle, WA, USA. [7]Present address: Cooperative Institute for Climate, Ocean, and Ecosystem Studies, University of Washington, Seattle, WA, USA. ✉e-mail: dbonan@uw.edu

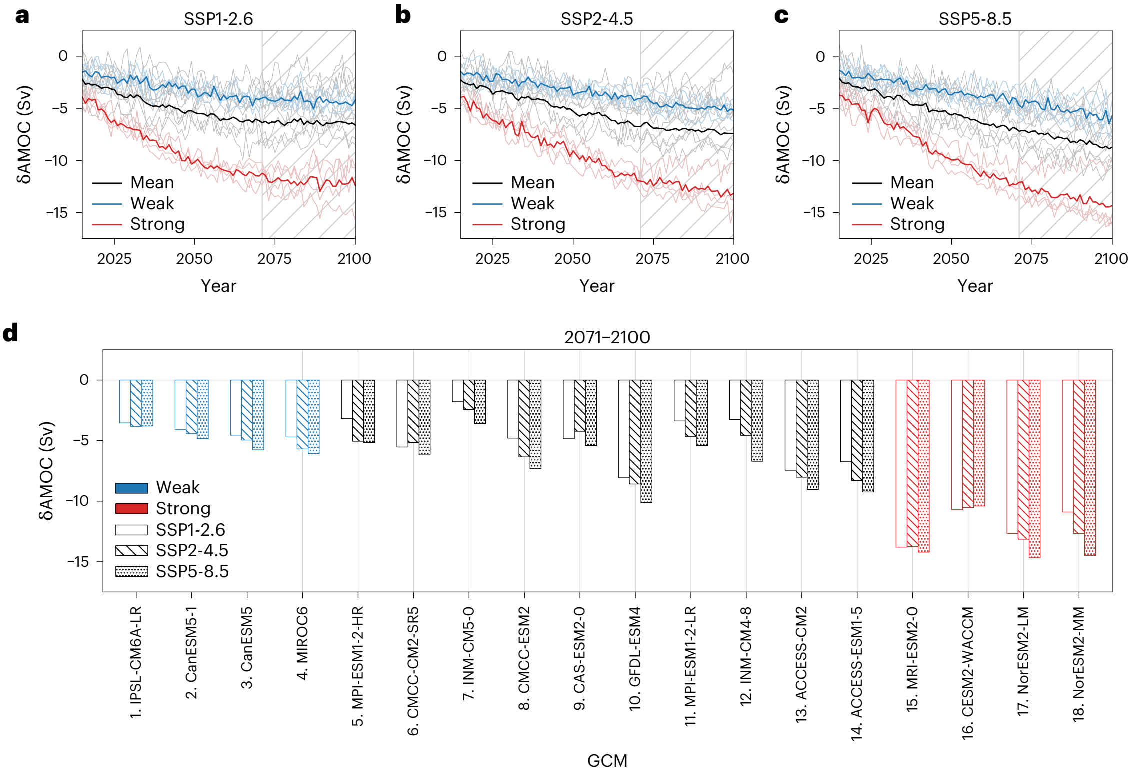

Fig. 1 | Relationship between the present-day and future AMOC strength. **a**–**c**, Time series of the change in AMOC strength for GCMs participating in CMIP6 under SSP1-2.6 (**a**), SSP2-4.5 (**b**) and SSP5-8.5 (**c**) emissions scenarios. The thick lines denote the averages of the four GCMs with the strongest present-day AMOC (red), the four GCMs with the weakest present-day AMOC (blue) and all GCMs (black). Each thin line denotes an individual GCM. The start year in **a**–**c** is 2015. **d**, The change in AMOC strength for GCMs under SSP1-2.6 (open bar), SSP2-4.5 (hatched bar) and SSP5-8.5 (dotted bar) emissions scenarios. The present-day time period is 1981–2010 and the SSP period is 2071–2100, as indicated by the grey hatches in **a**–**c**. GCMs in **d** are ordered from weak to strong present-day AMOC.

Intercomparison Project (CMIP6)[20] on average predict that, by the end of the century, the AMOC will weaken by about 8 Sv (1 Sv ≡ 10^6 m^3 s^{-1}; black line, Fig. 1). However, some GCMs predict that the AMOC will weaken by as little as 2 Sv, while others predict a more substantial weakening of up to 15 Sv (Fig. 1). Interestingly, the magnitude of AMOC weakening depends more on the specific GCM than on the emissions scenario (Fig. 1d).

How does the intermodel spread in AMOC projections arise? Over the past few decades, a series of studies have identified a strong correlation between the present-day AMOC strength and AMOC weakening under warming[4,21–26]. In particular, GCMs with a stronger present-day AMOC exhibit larger AMOC weakening. Indeed, the CMIP6 GCMs with the strongest present-day (1981–2010) AMOC tend to exhibit the largest AMOC weakening, predicting a decrease of 10–15 Sv by the end of the twenty-first century (red lines and bars, Fig. 1). Similarly, the CMIP6 GCMs with the weakest present-day AMOC tend to exhibit the smallest AMOC weakening, predicting a decrease of 3–6 Sv by the end of the twenty-first century (blue lines and bars, Fig. 1). This implies that the observed AMOC strength can be used to estimate the magnitude of AMOC weakening expected in the twenty-first century through an 'emergent constraint', which describes a statistical relationship between aspects of the present-day climate and future changes across GCMs. When combined with observations, emergent constraints can be used to reduce uncertainty in future climate projections.

Leveraging any emergent constraint to reduce uncertainty in future climate projections, however, requires a solid understanding of the underlying mechanisms on which the constraint depends[27]. In this case, the mechanisms underpinning the correlation between the present-day AMOC strength and future AMOC weakening have remained unclear. It has been suggested that the present-day AMOC relates to AMOC weakening under warming through subsurface stratification in the Labrador Sea, as GCMs with smaller present-day Labrador Sea stratification tend to show larger AMOC weakening[26]. Yet this explanation for AMOC weakening is incomplete as the Labrador Sea makes a limited contribution to dense water formation in most GCMs[28], and it is unclear how the Labrador Sea stratification affects volume transport associated with the AMOC. It is also unclear whether the relationship underpinning this emergent constraint is linear, which could affect constrained estimates of AMOC weakening[4]. A better understanding of the connection between the present-day AMOC and its projected changes is necessary to constrain twenty-first-century AMOC projections.

In this Article, we present a physical mechanism that explains how the present-day AMOC strength relates to AMOC weakening under warming. The mechanism is rooted in thermal-wind balance, which connects the AMOC strength to the magnitude of the meridional density difference and overturning depth in the Atlantic basin[29]. We show that the primary source of intermodel spread in AMOC weakening arises from changes in the overturning depth. The overturning depth also links the present-day and future AMOC strengths. In GCMs with a stronger and deeper present-day AMOC, the AMOC tends to weaken and shoal more under warming. This occurs because the present-day North Atlantic in these GCMs is less stratified, which allows for larger density changes at depth and leads to larger AMOC weakening. We use this relation and observations to constrain future AMOC projections and demonstrate that irrespective of the emissions scenario, the AMOC will probably experience limited weakening over the twenty-first century. Our approach builds on recent efforts[30] and addresses how the North Atlantic stratification affects AMOC weakening by influencing the vertical structure of meridional density gradients and the penetration of convective motions into the ocean interior[31,32].

Controls on Atlantic overturning circulation weakening

The depth-varying AMOC transport can be related to the vertical structure of the meridional density gradient through thermal-wind balance[33], which has been shown to reproduce the AMOC strength in comprehensive GCMs[29,30,34–36]. Thermal-wind balance links the meridional density gradient to zonal volume transport, which is associated with meridional volume transport through mass conservation. The vertical structure of the meridional density gradient can be decomposed into two factors[37], representing a characteristic magnitude of the meridional density difference between the high- and low-latitude Atlantic, $\langle \Delta_y \rho \rangle$, where y refers to the meridional direction, and a characteristic overturning depth, H. Note the angle brackets denote a vertical average of the upper ocean (discussed later in more detail). The AMOC strength ψ in terms of these factors can be expressed as

$$\psi = \frac{g}{2\rho_0 f_0} \langle \Delta_y \rho \rangle H^2, \tag{1}$$

where $g = 9.81\ \mathrm{m\ s^{-2}}$ is the gravitational acceleration, $\rho_0 = 1{,}027.5\ \mathrm{kg\ m^{-3}}$ is a reference density of seawater, and $f_0 = 10^{-4}\ \mathrm{s^{-1}}$ is the Coriolis parameter near 40° N. The two key variables, $\langle \Delta_y \rho \rangle$ and H, can be diagnosed directly from CMIP6 output (Methods). Building on efforts by refs. 29,30, the variable $\langle \Delta_y \rho \rangle$ is calculated as the vertical average of the potential density difference between the North Atlantic (area-averaged from 40° N to 65° N) and the low-latitude Atlantic (area-averaged from 30° S to 30° N) over the upper 2,000 m of the ocean. This estimate of $\langle \Delta_y \rho \rangle$ represents the magnitude of the meridional density gradient in the upper cell. The variable H is calculated as the depth where the depth-integrated $\Delta_y \rho$ (for the same regional domains) equals the vertical mean of the depth-integrated $\Delta_y \rho$ over the entire water column. More specifically, H is calculated by defining the depth-integrated $\Delta_y \rho$ as

$$I(z) = \int_{-z}^{0} \Delta_y \rho(z) \mathrm{d}z, \tag{2}$$

where z is the depth in metres, and finding the depth H where $I(H)$ is equal to the vertical mean of equation (2) from the surface to D, where D is the depth of the entire water column. This estimate of H is approximately the depth of maximum zonal volume transport[29] and, assuming weak eastern boundary currents, can be thought of as the depth of maximum meridional volume transport. Equation (1) has previously been shown to approximate the AMOC strength in GCMs under pre-industrial climate conditions[30].

By linearizing equation (1), the change in AMOC strength $\delta\psi$ can be decomposed as

$$\delta\psi = \frac{g}{2\rho_0 f_0} \left(\underbrace{H^2 \delta \langle \Delta_y \rho \rangle}_{\text{(A)}} + \underbrace{2 \langle \Delta_y \rho \rangle H \delta H}_{\text{(B)}} + \underbrace{\epsilon}_{\text{(C)}} \right), \tag{3}$$

where (A) represents the AMOC strength change due to a change in $\langle \Delta_y \rho \rangle$; (B) represents the AMOC strength change due to a change in H; and (C) represents the AMOC strength change due to higher-order residual terms.

The thermal-wind expression (equation (3)) captures the AMOC weakening simulated by CMIP6 GCMs at the end of the twenty-first century. It accounts for approximately 75% of the intermodel variance in AMOC weakening (that is, $r^2 = 0.75$) and exhibits a root-mean-square error of approximately 2 Sv for each emissions scenario (Fig. 2a–c and Extended Data Fig. 1). Importantly, the thermal-wind expression correctly predicts the small and large AMOC weakening for GCMs with a weak and strong present-day AMOC, respectively (blue and red bars, Fig. 2).

The ability of the thermal-wind expression to capture the AMOC weakening in GCMs implies that H and $\langle \Delta_y \rho \rangle$ can explain why the present-day AMOC is related to the magnitude of AMOC weakening under warming. Term B, which represents the AMOC strength change due to δH, is responsible for the majority of the intermodel spread in AMOC weakening, accounting for 74%, 63% and 61% of the intermodel variance for the Shared Socioeconomic Pathway (SSP) 1-2.6, SSP2-4.5 and SSP5-8.5 emissions scenarios, respectively (hatched bars, Fig. 2a–c). Term B also shows that GCMs with a stronger present-day AMOC exhibit larger AMOC weakening (compare blue and red bars, Fig. 2). Term A, which represents the AMOC strength change due to $\delta\langle \Delta_y \rho \rangle$, accounts for a smaller fraction of intermodel variance: 33%, 25% and 16% for the SSP1-2.6, SSP2-4.5 and SSP5-8.5 emissions scenarios, respectively (open bars, Fig. 2a–c). While Term A contributes some to the AMOC weakening in each GCM, it contributes little to the relationship between the present-day and future AMOC strengths. In other words, Term A is similar in magnitude for GCMs with a weak (for example, IPSL-CM6A-LR) and strong (for example, NorESM2-MM) present-day AMOC. Term A is larger for higher emissions scenarios (for example, SSP5-8.5), but overall $\delta\langle \Delta_y \rho \rangle$ does not contribute much to the spread across GCMs (open bars, Fig. 2a–c).

Term B for each individual GCM is similar across the different emissions scenarios, indicating that the reason the AMOC weakens similarly across each emissions scenario can be related to δH (hatched bars, Fig. 2a–c). The intermodel spread in Term B arises from δH, with much smaller contributions from H and $\langle \Delta_y \rho \rangle$ (Extended Data Fig. 2). However, GCMs with a stronger present-day AMOC tend to have a larger overturning depth, H (ref. 30), suggesting that GCMs with larger H also experience larger shoaling under warming. In fact, H and δH across each emissions scenario are negatively correlated, with a Pearson correlation coefficient of $r \approx -0.61$, meaning GCMs with a larger present-day H exhibit more shoaling under warming.

To understand the processes contributing to δH and its relationship to H, we revisit equation (2) and examine changes to the vertical structure of $\Delta_y \rho(z)$, which determines the magnitude of δH. For the same column-averaged change in $\Delta_y \rho(z)$, a small reduction throughout the entire water column would result in more shoaling of H whereas a large reduction confined to the surface ocean would lead to less shoaling of H. Scaling arguments also suggest that H is inversely related to the stratification (N^2) of the North Atlantic[30], meaning that a smaller present-day H is associated with a larger present-day N^2. A larger present-day North Atlantic N^2 would limit δH by inhibiting the vertical penetration of surface buoyancy flux anomalies that can alter the vertical structure of $\Delta_y \rho(z)$.

Indeed, GCMs with a weaker present-day AMOC also tend to have a larger present-day N^2 in the North Atlantic (Fig. 3a), with $r \approx -0.89$. GCMs with a larger present-day North Atlantic N^2 also exhibit smaller AMOC weakening under each emissions scenario, with $r \approx 0.66$. This suggests a connection between the present-day North Atlantic N^2 and AMOC weakening via δH. The connection between these components becomes more evident in vertical profiles of the North Atlantic (40° N–65° N) density change, which contributes most to the change in $\Delta_y \rho(z)$ and thus δH. Grouping together GCMs with a strong present-day AMOC (red) and a weak present-day AMOC (blue) shows that a strong present-day AMOC (and thus small present-day North Atlantic N^2) corresponds to larger density changes at depth and more vertically uniform North Atlantic density changes (red lines, Fig. 3b–d). In particular, for GCMs with a strong present-day AMOC, density changes between 1,000 and 2,000 m are of more comparable magnitude to density changes between 0 and 200 m, consistent with deeper mixing of surface buoyancy flux anomalies (red lines, Fig. 3b–d). By contrast, GCMs with a weak present-day AMOC (and large present-day North Atlantic N^2) tend to exhibit smaller North Atlantic density changes at depth and larger density changes at the surface, indicating shallower mixing of surface buoyancy flux anomalies (blue lines, Fig. 3b–d). For SSP5-8.5 (the higher emissions

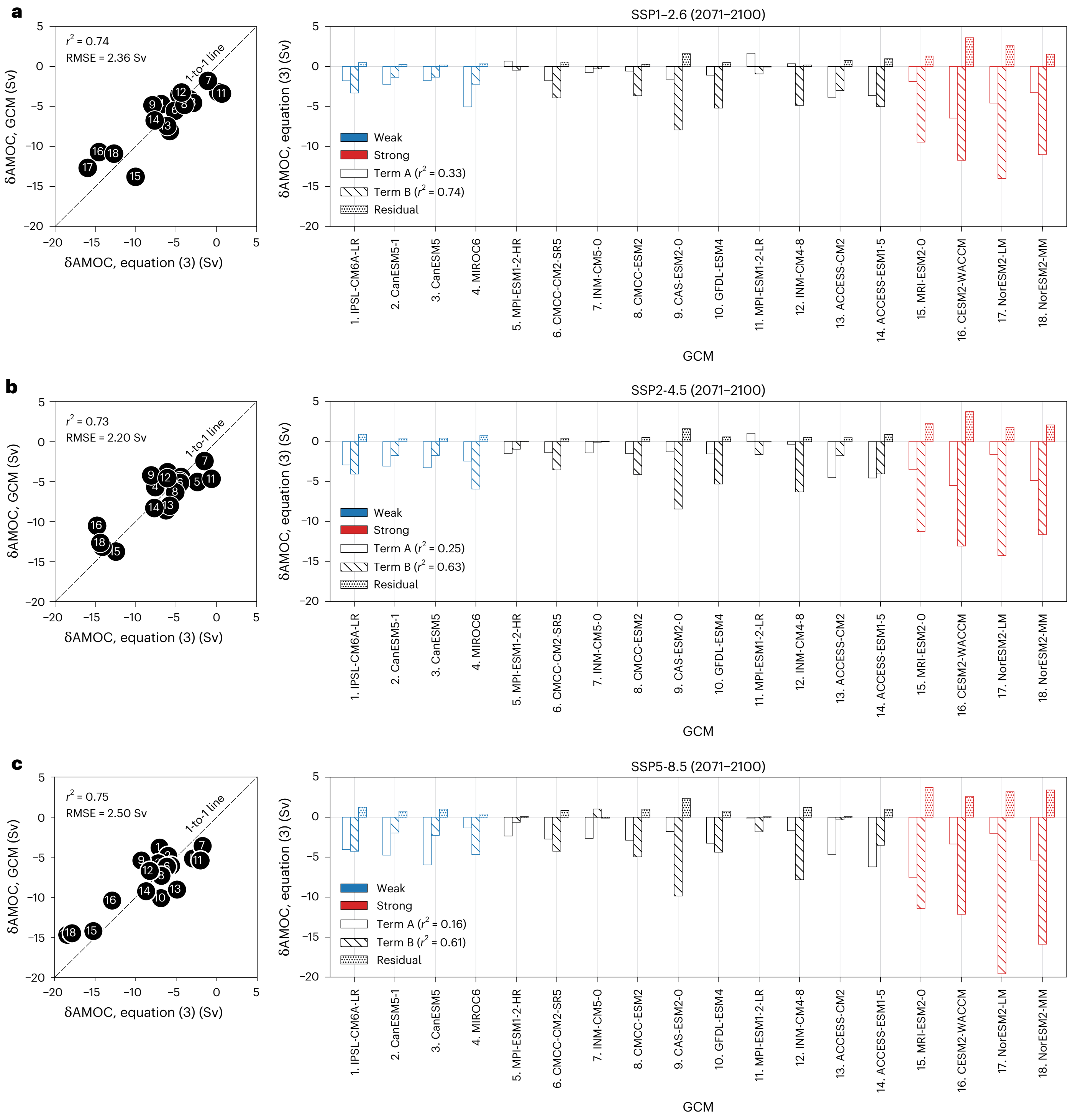

Fig. 2 | Controls on AMOC weakening at the end of the twenty-first century. **a**–**c**, Change in the AMOC strength for SSP1-2.6 (**a**), SSP2-4.5 (**b**) and SSP5-8.5 (**c**) emissions scenarios. The scatter plots on the left show a comparison of (*x* axis) the AMOC strength change predicted by the thermal-wind expression (equation (3)) and (*y* axis) the AMOC strength change in GCMs. The proportion of variance accounted for and root-mean-square error are shown in the top left part of each panel. The bar plots on the right show the AMOC strength change predicted by Term A (white bar), Term B (hatched bar) and the higher-order residual terms (dotted bar) in the thermal-wind expression (equation (3)). Term A represents changes in the magnitude of the Atlantic basin meridional density difference $\langle \Delta_y \rho \rangle$, and Term B represents changes in the overturning depth H. The proportion of variance accounted for by each term is shown in the legend of each panel. The present-day period is 1981–2010, and the SSP period is 2070–2100. GCMs are ordered from weak to strong present-day AMOC.

scenario), all GCMs exhibit large density changes near the surface, but GCMs with a smaller or larger present-day North Atlantic N^2 still tend to exhibit larger or smaller density changes at depth, respectively.

The preceding results demonstrate that the present-day North Atlantic N^2 strongly influences the vertical structure of density changes, which determines the magnitude of AMOC weakening through δH. In other words, twenty-first-century AMOC weakening can be related to the present-day Atlantic stratification. This finding is consistent with ref. 26 and further illustrates how present-day stratification can result in a change in AMOC volume transport. These results can be

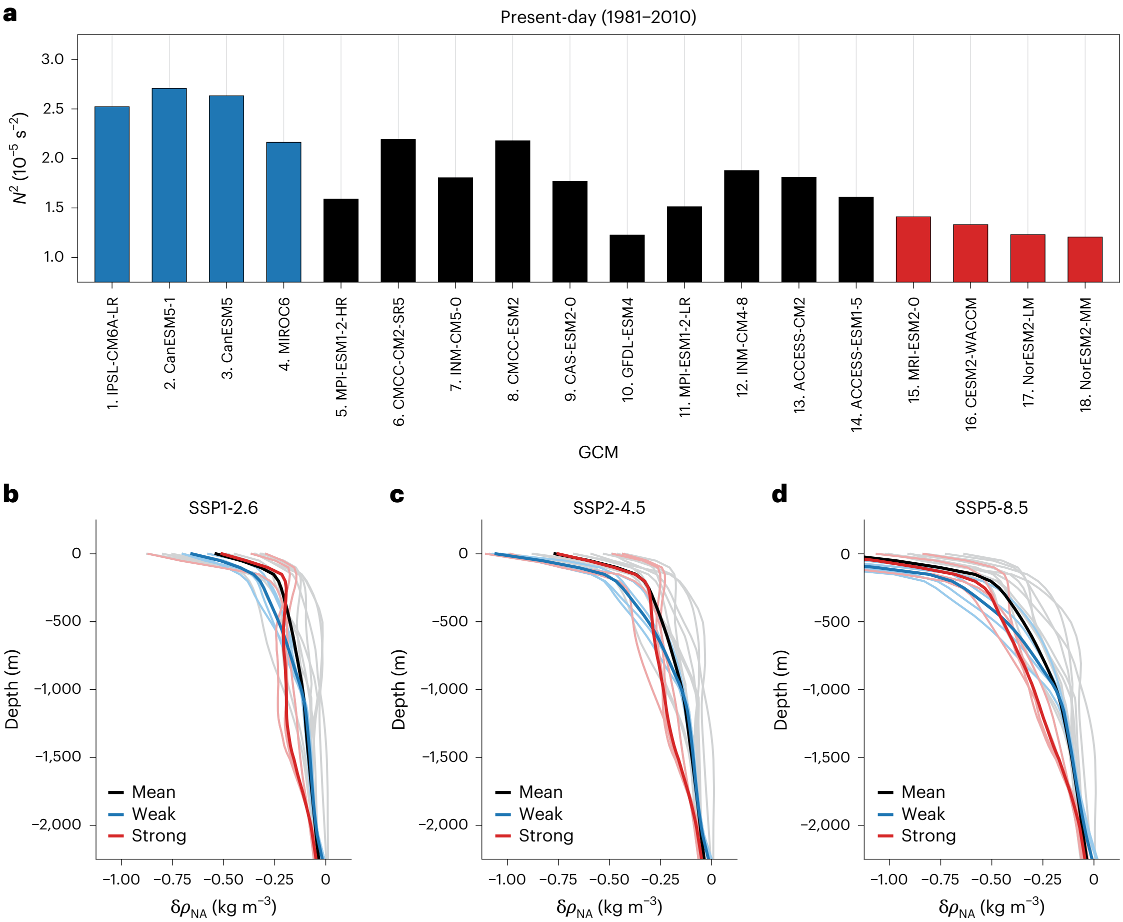

Fig. 3 | Relationship between present-day and future North Atlantic stratification. a, The present-day stratification (N^2) of the North Atlantic (40° N–65° N, 50–1,000 m) from CMIP6 historical simulations. GCMs are ordered from weak to strong present-day AMOC. **b**–**d**, The change in the North Atlantic density ($\delta\rho_{NA}$) as a function of depth for SSP1-2.6 (**b**), SSP2-4.5 (**c**) and SSP5-8.5 (**d**) emissions scenarios between the present-day period, 1981–2010, and the SSP period, 2071–2100. The thick lines denote the averages of the four GCMs with the strongest present-day AMOC (red), the four GCMs with the weakest present-day AMOC (blue) and all GCMs (black). Each thin line denotes an individual GCM.

summarized by schematics depicting GCMs with a weak present-day AMOC (Fig. 4a) and a strong present-day AMOC (Fig. 4b). In GCMs with a weak present-day AMOC, the AMOC tends to be shallow (smaller H) and the North Atlantic tends to be strongly stratified (larger N^2). Under warming, any change to ocean density from surface buoyancy flux anomalies will occur closer to the surface and will not penetrate deeply into the interior of the North Atlantic, leading to smaller density changes at depth. This results in a smaller δH and thus smaller AMOC weakening. By contrast, in GCMs with a strong present-day AMOC, the AMOC tends to be deeper (larger H), and the North Atlantic tends to be weakly stratified (smaller N^2). Under warming, the same surface buoyancy flux anomalies will penetrate more deeply into the interior of the North Atlantic, leading to larger density changes at depth. This results in a larger δH and, therefore, a larger weakening of the AMOC.

Constraints on Atlantic overturning circulation weakening

We can now leverage this mechanistic understanding of AMOC weakening to constrain twenty-first-century AMOC projections (Methods). The unconstrained probability density function (PDF) of CMIP6 projections suggests that, regardless of the emissions scenario, the AMOC most likely will weaken by about 8 ± 3 Sv (1 standard deviation) at the end of the twenty-first century (black PDFs, Fig. 5). However, there is considerable intermodel spread, with some likelihood of a substantial AMOC weakening of ~15 Sv.

The previously identified relationship between the present-day and future AMOC strength can be used to constrain AMOC projections by incorporating present-day observations[4]. The AMOC strength diagnosed from the observationally constrained Estimating the Circulation and Climate of the Ocean (ECCO) state estimate[38] and linear regression of the present-day AMOC against the future AMOC change (Methods) suggests that the AMOC will weaken by only about 4 ± 1.5 Sv (1 standard deviation) at the end of the twenty-first century (blue PDFs, Fig. 5). The likelihood of a large AMOC weakening is substantially reduced, with an AMOC decline exceeding 9 Sv being extremely unlikely based on the Intergovernmental Panel on Climate Change likelihood scale (probability <5%) for all emissions scenarios (blue PDFs, solid lines, Fig. 5). Using an alternative estimate of the observed AMOC strength derived from the RAPID mooring array[39] (Methods), which suggests that the present-day AMOC is slightly stronger (Extended Data Fig. 3), results in a constrained weakening estimate of approximately 5 ± 2 Sv (blue PDFs, dashed lines, Fig. 5). Although this constrained estimate is slightly higher than the value based on the ECCO-derived AMOC strength, it still indicates limited weakening of the AMOC compared with unconstrained projections.

Can we trust the linear relationship between the present-day and future AMOC strengths? Considering that thermal-wind balance accounts for a large portion of the intermodel variance in AMOC weakening, we can examine the linear assumption by constructing a simple physical expression that links the present-day and future

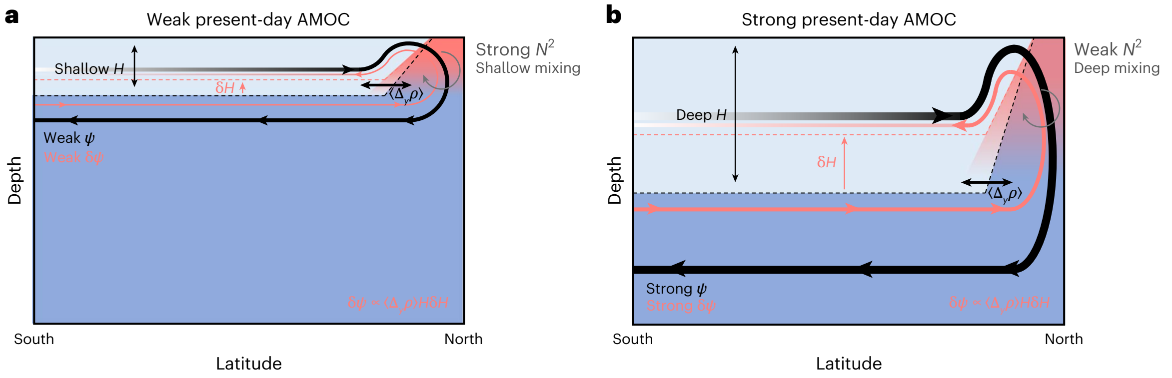

Fig. 4 | Schematic depicting the processes linking the present-day and future AMOC strength. a,**b**, Processes that contribute to AMOC weakening under warming for GCMs with a weak present-day AMOC (**a**) and a strong present-day AMOC (**b**). The dashed black line denotes the present-day overturning depth (H). The black double-sided arrows and colours of each isopycnal layer denote the magnitude of the present-day meridional density difference ($\langle\Delta_y\rho\rangle$). The black streamline denotes the present-day AMOC (ψ). The grey arrows denote the magnitude of present-day North Atlantic stratification (N^2), which limits mixing deep into the interior of the North Atlantic. GCMs with a deeper present-day H tend to have a stronger present-day AMOC and weaker present-day N^2, which enables H to shoal more under warming (as indicated by the red dashed line), resulting in larger AMOC weakening (as indicated by the red streamline, which denotes the AMOC strength change). In other words, a stronger present-day AMOC and weaker present-day N^2 allow for deeper mixing of surface buoyancy flux anomalies into the North Atlantic water column (as indicated by the red shading) and result in larger shoaling and weakening of the AMOC through larger density changes at depth. The dominant term in equation (3) is shown in the bottom right-hand corner of each plot.

AMOC strengths. The AMOC strength change $\delta\psi$ based on the thermal-wind expression can be attributed mainly to Term B in equation (3), resulting in

$$\delta\psi \approx \frac{g}{\rho_0 f_0}\overline{\langle\Delta_y\rho\rangle}H\delta H, \tag{4}$$

where the overline indicates the multimodel mean value of $\langle\Delta_y\rho\rangle$. We use the multimodel mean $\langle\Delta_y\rho\rangle$ and ignore Term A in equation (3) because both contribute relatively little to the intermodel spread in AMOC weakening. Furthermore, because δH depends on H and $\overline{\langle\Delta_y\rho\rangle}$ is a constant, the preceding expression can be related to the present-day AMOC strength ψ via regression analysis of H and δH, which results in

$$\delta\psi \approx \frac{g}{\rho_0 f_0}\overline{\langle\Delta_y\rho\rangle}H(\psi)\left[a_H + b_H H(\psi)\right], \tag{5}$$

where a_H is the intercept and b_H is the slope of the linear regression of δH on H. Because we have assumed that $\langle\Delta_y\rho\rangle$ is a constant, ψ is a function of H only (equation (1)), enabling us to invert H and make it a function of ψ, which results in

$$H(\psi) = \sqrt{\frac{2\rho_0 f_0 \psi}{g\overline{\langle\Delta_y\rho\rangle}}}. \tag{6}$$

Equation (5) predicts $\delta\psi$ from ψ via H and thus provides a physical understanding of the statistical relationship between the present-day and future AMOC strengths in GCMs. More specifically, equations (5) and (6) show that it is H, a measure of the AMOC depth, that connects the present-day and future AMOC strengths and that this relationship includes a nonlinear term.

The physically based expressions provide an additional estimate of twenty-first-century AMOC weakening. Together, equations (5) and (6) better predict the larger AMOC weakening in GCMs with a strong present-day AMOC, compared with the linear regression of future AMOC change based on the present-day AMOC strength (see orange and blue lines in Fig. 5). Specifically, equations (5) and (6) capture the nonlinear AMOC weakening, showing larger weakening in GCMs with a stronger present-day AMOC (compare orange and blue regression lines in Fig. 5). This nonlinear weakening occurs because $\delta\psi$ in equation (5) includes both a term proportional to ψ and a term proportional to $\psi^{1/2}$. Using the PDF of observed AMOC strength from ECCO along with the prediction of $\delta\psi$ from equations (5) and (6) (Methods) provides an additional estimate of future AMOC weakening (orange PDFs, Fig. 5). The constrained estimate also suggests that the AMOC will weaken by about 4 ± 1.5 Sv (1 standard deviation) by 2071–2100 under all emissions scenarios.

These results show that because some GCMs simulate a stronger present-day AMOC relative to observations, they also simulate excessive AMOC weakening over the twenty-first century. This emergent constraint, which we derive from physical principles, corrects these biases and suggests limited AMOC weakening over the twenty-first century. An AMOC weakening of approximately 3–6 Sv represents a decline of approximately 18–43% relative to the observed AMOC strength.

Implications for twenty-first-century climate projections

In recent years, several studies have raised concerns about a potential collapse of the AMOC in the twenty-first century[40–42]. These studies argue that independent proxies for the AMOC strength indicate either bi-stable AMOC states or early warnings of AMOC instability in the present-day climate. However, it has also been argued that some of these studies, particularly those employing statistical models[41], may produce false alarms of an AMOC collapse[43]. While our study does not directly investigate indicators of AMOC collapse, our findings suggest an AMOC collapse during the twenty-first century is unlikely. In fact, our approach, which uses a physically based relation instead of a statistical model, suggests that AMOC weakening over the twenty-first century, as simulated by contemporary GCMs, will be limited.

The emergent constraint framework assumes that GCMs simulate all relevant processes that govern the relationship between present-day and future AMOC strengths. This assumption could be the reason our conclusions imply limited AMOC weakening. For example, it is argued that contemporary GCMs suffer from a freshwater transport bias that favours a stable AMOC[40,44–46]. This model bias also affects the stratification of the Atlantic basin and potentially the relationship between H and δH. Reference 40 corrected this freshwater transport bias in a comprehensive GCM and showed that the AMOC would eventually collapse, although this occurred a few centuries after the

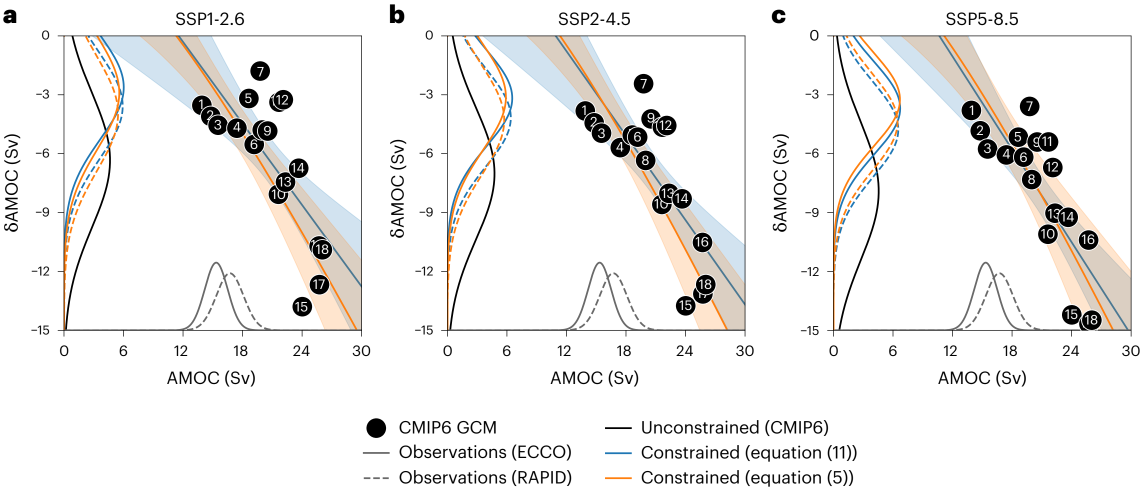

Fig. 5 | Constraints on AMOC weakening at the end of the twenty-first century. **a**–**c**, Scatter plot of the present-day (1981–2010) AMOC strength (*x* axis) versus the change in AMOC strength (*y* axis) under (SSP1-2.6 (**a**), SSP2-4.5 (**b**) and SSP5-8.5 (**c**) emissions scenarios for years 2071–2100. Each dot denotes a GCM (see Figs. 1–3 for model number and model name). The blue line and shading in each panel denote the linear regression and two standard deviations of the linear regressions, respectively. The orange line in each panel denotes equation (5), which predicts the AMOC strength change on the basis of present-day *H* via equation (6). The orange shading in each panel denotes the two standard deviations of the linear regressions between *H* and δ*H*. The grey probability distributions denote observational estimates of the AMOC strength from ECCO (solid) and the RAPID array (dashed). The black probability distributions denote the change in AMOC strength for years 2071–2100 using unconstrained CMIP6 GCMs. The blue probability distributions denote the change in AMOC strength for years 2071–2100 using CMIP6 GCMs constrained by equation (11) and observational estimates of the AMOC strength from ECCO (solid) and the RAPID array (dashed). The orange probability distributions denote the change in AMOC strength for years 2071–2100 using CMIP6 GCMs constrained by equations (5) and (6) and observational estimates of the AMOC strength from ECCO (solid) and the RAPID array (dashed).

abrupt forcing, suggesting no imminent collapse in the twenty-first century. Furthermore, our results, which show limited AMOC weakening over the twenty-first century, may change as comprehensive GCMs begin to include additional climate processes, such as ice-sheet freshwater fluxes, which have been shown to cause additional AMOC weakening[47,48] and are not currently represented in the GCMs used in this study.

The key takeaway from this work is that the well-known relationship between the present-day AMOC strength and its future weakening can be explained by thermal-wind balance. GCMs that exhibit a stronger and deeper present-day AMOC tend to predict larger weakening and shoaling under warming. This occurs because the present-day North Atlantic in these GCMs is less stratified, allowing surface buoyancy flux changes to penetrate more deeply, leading to larger density changes at depth and, consequently, larger AMOC weakening. Incorporating observational constraints with this physical explanation suggests that the AMOC will undergo limited weakening over the twenty-first century. This work also explains why the uncertainty in twenty-first-century AMOC projections arises more from intermodel differences than from differences in SSP emissions scenarios (Fig. 1): the extent of twenty-first-century AMOC weakening is most sensitive to the present-day Atlantic basin stratification, which varies considerably among GCMs. This study adds to a growing body of work that indicates the behaviour of the ocean under transient climate change is closely tied to the background ocean state[25,49,50]. Therefore, improving the representation of processes that determine the present-day ocean state will also likely improve twenty-first-century climate projections.

Online content

Any methods, additional references, Nature Portfolio reporting summaries, source data, extended data, supplementary information, acknowledgements, peer review information; details of author contributions and competing interests; and statements of data and code availability are available at https://doi.org/10.1038/s41561-025-01709-0.

References

1. Schmittner, A., Latif, M. & Schneider, B. Model projections of the North Atlantic thermohaline circulation for the 21st century assessed by observations. *Geophys. Res. Lett.* **32** (2005).
2. Cheng, W., Chiang, J. C. & Zhang, D. Atlantic meridional overturning circulation (AMOC) in CMIP5 models: RCP and historical simulations. *J. Clim.* **26**, 7187–7197 (2013).
3. Reintges, A., Martin, T., Latif, M. & Keenlyside, N. S. Uncertainty in twenty-first century projections of the Atlantic meridional overturning circulation in CMIP3 and CMIP5 models. *Clim. Dyn.* **49**, 1495–1511 (2017).
4. Weijer, W., Cheng, W., Garuba, O. A., Hu, A. & Nadiga, B. CMIP6 models predict significant 21st century decline of the Atlantic meridional overturning circulation. *Geophys. Res. Lett.* **47**, e2019GL086075 (2020).
5. Buckley, M. W. & Marshall, J. Observations, inferences, and mechanisms of the Atlantic meridional overturning circulation: a review. *Rev. Geophys.* **54**, 5–63 (2016).
6. Ganachaud, A. & Wunsch, C. Large-scale ocean heat and freshwater transports during the World Ocean Circulation Experiment. *J. Clim.* **16**, 696–705 (2003).
7. Zhang, R. & Delworth, T. L. Impact of Atlantic multidecadal oscillations on India/Sahel rainfall and Atlantic hurricanes. *Geophys. Res. Lett.* **33** (2006).
8. Zhang, R. et al. A review of the role of the Atlantic meridional overturning circulation in Atlantic multidecadal variability and associated climate impacts. *Rev. Geophys.* **57**, 316–375 (2019).
9. Mahajan, S., Zhang, R. & Delworth, T. L. Impact of the Atlantic meridional overturning circulation (AMOC) on Arctic surface air temperature and sea ice variability. *J. Clim.* **24**, 6573–6581 (2011).
10. Day, J. J., Hargreaves, J., Annan, J. & Abe-Ouchi, A. Sources of multi-decadal variability in Arctic sea ice extent. *Environ. Res. Lett.* **7**, 034011 (2012).

11. Frierson, D. M. et al. Contribution of ocean overturning circulation to tropical rainfall peak in the Northern Hemisphere. *Nat. Geosci.* **6**, 940–944 (2013).
12. Schneider, T., Bischoff, T. & Haug, G. H. Migrations and dynamics of the intertropical convergence zone. *Nature* **513**, 45–53 (2014).
13. Marshall, J., Donohoe, A., Ferreira, D. & McGee, D. The ocean's role in setting the mean position of the Inter-Tropical Convergence Zone. *Clim. Dyn.* **42**, 1967–1979 (2014).
14. Yin, J., Griffies, S. M. & Stouffer, R. J. Spatial variability of sea level rise in twenty-first century projections. *J. Clim.* **23**, 4585–4607 (2010).
15. Gregory, J. M. et al. The Flux-Anomaly-Forced Model Intercomparison Project (FAFMIP) contribution to CMIP6: investigation of sea-level and ocean climate change in response to CO_2 forcing. *Geosci. Model Dev.* **9**, 3993–4017 (2016).
16. Saenko, O. A., Yang, D. & Myers, P. G. Response of the North Atlantic dynamic sea level and circulation to Greenland meltwater and climate change in an eddy-permitting ocean model. *Clim. Dyn.* **49**, 2895–2910 (2017).
17. Vellinga, M. & Wood, R. A. Impacts of thermohaline circulation shutdown in the twenty-first century. *Clim. Change* **91**, 43–63 (2008).
18. Jackson, L. et al. Global and European climate impacts of a slowdown of the AMOC in a high resolution GCM. *Clim. Dyn.* **45**, 3299–3316 (2015).
19. Liu, W., Fedorov, A. V., Xie, S.-P. & Hu, S. Climate impacts of a weakened Atlantic meridional overturning circulation in a warming climate. *Sci. Adv.* **6**, eaaz4876 (2020).
20. Eyring, V. et al. Overview of the Coupled Model Intercomparison Project Phase 6 (CMIP6) experimental design and organization. *Geosci. Model Dev.* **9**, 1937–1958 (2016).
21. Gregory, J. et al. A model intercomparison of changes in the Atlantic thermohaline circulation in response to increasing atmospheric CO_2 concentration. *Geophys. Res. Lett.* **32** (2005).
22. Gregory, J. M. & Tailleux, R. Kinetic energy analysis of the response of the Atlantic meridional overturning circulation to CO_2-forced climate change. *Clim. Dyn.* **37**, 893–914 (2011).
23. Weaver, A. J. et al. Stability of the Atlantic meridional overturning circulation: a model intercomparison. *Geophys. Res. Lett.* **39** (2012).
24. Kostov, Y., Armour, K. C. & Marshall, J. Impact of the Atlantic meridional overturning circulation on ocean heat storage and transient climate change. *Geophys. Res. Lett.* **41**, 2108–2116 (2014).
25. Winton, M. et al. Has coarse ocean resolution biased simulations of transient climate sensitivity? *Geophys. Res. Lett.* **41**, 8522–8529 (2014).
26. Lin, Y.-J., Rose, B. E. & Hwang, Y.-T. Mean state AMOC affects AMOC weakening through subsurface warming in the Labrador Sea. *J. Clim.* **36**, 3895–3915 (2023).
27. Hall, A., Cox, P., Huntingford, C. & Klein, S. Progressing emergent constraints on future climate change. *Nat. Clim. Change* **9**, 269–278 (2019).
28. Jackson, L. & Petit, T. North Atlantic overturning and water mass transformation in CMIP6 models. *Clim. Dyn.* **60**, 2871–2891 (2023).
29. De Boer, A. M., Gnanadesikan, A., Edwards, N. R. & Watson, A. J. Meridional density gradients do not control the Atlantic overturning circulation. *J. Phys. Oceanogr.* **40**, 368–380 (2010).
30. Nayak, M. S., Bonan, D. B., Newsom, E. R. & Thompson, A. F. Controls on the strength and structure of the Atlantic meridional overturning circulation in climate models. *Geophys. Res. Lett.* **51**, e2024GL109055 (2024).
31. Spall, M. A. Boundary currents and watermass transformation in marginal seas. *J. Phys. Oceanogr.* **34**, 1197–1213 (2004).
32. Buckley, M. W., Lozier, M. S., Desbruyères, D. & Evans, D. G. Buoyancy forcing and the subpolar Atlantic meridional overturning circulation. *Phil. Trans. R. Soc. A* **381**, 20220181 (2023).
33. Nikurashin, M. & Vallis, G. A theory of the interhemispheric meridional overturning circulation and associated stratification. *J. Phys. Oceanogr.* **42**, 1652–1667 (2012).
34. Jansen, M. F., Nadeau, L.-P. & Merlis, T. M. Transient versus equilibrium response of the ocean's overturning circulation to warming. *J. Clim.* **31**, 5147–5163 (2018).
35. Sigmond, M., Fyfe, J. C., Saenko, O. A. & Swart, N. C. Ongoing AMOC and related sea-level and temperature changes after achieving the Paris targets. *Nat. Clim. Change* **10**, 672–677 (2020).
36. Bonan, D. B., Thompson, A. F., Newsom, E. R., Sun, S. & Rugenstein, M. Transient and equilibrium responses of the Atlantic overturning circulation to warming in coupled climate models: the role of temperature and salinity. *J. Clim.* **35**, 5173–5193 (2022).
37. Johnson, H. L., Marshall, D. P. & Sproson, D. A. Reconciling theories of a mechanically driven meridional overturning circulation with thermohaline forcing and multiple equilibria. *Clim. Dyn.* **29**, 821–836 (2007).
38. Forget, G. et al. ECCO version 4: an integrated framework for non-linear inverse modeling and global ocean state estimation. *Geosci. Model Dev.* **8**, 3071–3104 (2015).
39. Cunningham, S. A. et al. Temporal variability of the Atlantic meridional overturning circulation at 26.5° N. *Science* **317**, 935–938 (2007).
40. Liu, W., Xie, S.-P., Liu, Z. & Zhu, J. Overlooked possibility of a collapsed Atlantic meridional overturning circulation in warming climate. *Sci. Adv.* **3**, e1601666 (2017).
41. Boers, N. Observation-based early-warning signals for a collapse of the Atlantic meridional overturning circulation. *Nat. Clim. Change* **11**, 680–688 (2021).
42. Ditlevsen, P. & Ditlevsen, S. Warning of a forthcoming collapse of the Atlantic meridional overturning circulation. *Nat. Commun.* **14**, 4254 (2023).
43. Chen, X. & Tung, K.-K. Evidence lacking for a pending collapse of the Atlantic meridional overturning circulation. *Nat. Clim. Change* **14**, 40–42 (2024).
44. Hofmann, M. & Rahmstorf, S. On the stability of the Atlantic meridional overturning circulation. *Proc. Natl Acad. Sci. USA* **106**, 20584–20589 (2009).
45. Mecking, J., Drijfhout, S., Jackson, L. & Andrews, M. The effect of model bias on Atlantic freshwater transport and implications for AMOC bi-stability. *Tellus A* **69**, 1299910 (2017).
46. Van Westen, R. M. & Dijkstra, H. A. Persistent climate model biases in the Atlantic Ocean's freshwater transport. *Ocean Sci.* **20**, 549–567 (2024).
47. Lenaerts, J. T. et al. Representing Greenland ice sheet freshwater fluxes in climate models. *Geophys. Res. Lett.* **42**, 6373–6381 (2015).
48. Bakker, P. et al. Fate of the Atlantic meridional overturning circulation: strong decline under continued warming and Greenland melting. *Geophys. Res. Lett.* **43**, 12–252 (2016).
49. He, J., Winton, M., Vecchi, G., Jia, L. & Rugenstein, M. Transient climate sensitivity depends on base climate ocean circulation. *J. Clim.* **30**, 1493–1504 (2017).
50. Newsom, E., Zanna, L. & Gregory, J. Background pycnocline depth constrains future ocean heat uptake efficiency. *Geophys. Res. Lett.* **50**, e2023GL105673 (2023).

Methods

CMIP6 output

This analysis includes all CMIP6 models[20] from the r1i1p1f1 variant label that provide monthly output of ocean potential temperature (thetao), ocean absolute salinity (so) and the meridional overturning streamfunction (msftmz or msftmy) for historical, SSP1-2.6, SSP2-4.5 and SSP5-8.5 emissions scenarios. Model names are provided in Figs. 1–3. The present-day climatological period is 1981–2010, and the SSP climatological period is 2071–2100. The AMOC strength is defined as the maximum value of the meridional overturning streamfunction in the Atlantic basin northwards of 30° S and below 500 m. The choice of 500 m avoids volume flux contributions associated with the subtropical ocean gyres. This definition of the AMOC strength results in maximum values between 30° N and 45° N. This definition of the AMOC strength also results in a stronger correlation between the present-day and future AMOC strengths when compared using a fixed latitude (for example, 26.5° N). Ocean potential density is calculated from ocean potential temperature and ocean absolute salinity and referenced to 2,000 dbar using the Gibbs SeaWater Oceanographic Toolbox of TEOS-10[51]. The Brunt–Väisälä frequency N^2 is calculated from ocean potential density ρ as

$$N^2 = -\frac{g}{\rho_0}\frac{\partial \rho}{\partial z}, \tag{7}$$

and used to indicate stratification of the North Atlantic. The North Atlantic stratification is first calculated at each discrete depth level and then averaged over the depth range of 50–1,000 m and latitude range of 40° N–65° N.

Observations

Observational estimates of the AMOC strength are obtained from two different datasets. The first dataset comes from the ECCOV4r3 (ECCO) state estimate[38]. ECCO is based on the MITgcm ocean model[52] at 1° resolution with 50 vertical levels. The state estimate is iteratively improved by modifying ocean model initial conditions, parameters and atmospheric boundary conditions to minimize model–observation disagreement. The AMOC strength in ECCO is defined as the maximum value of the meridional overturning streamfunction in the Atlantic basin polewards of 30° S and below 500 m. The second dataset comes from the Rapid Meridional Overturning Circulation (RAPID) mooring array[39], which was deployed in 2004 to continuously monitor the meridional overturning circulation in the Atlantic basin at 26.5°N. However, to be consistent with the definition of the AMOC strength in the CMIP6 GCMs, we use primarily ECCO as an observational estimate of the AMOC. In other words, because we define the AMOC strength in each GCM as the maximum value of the meridional overturning streamfunction in the Atlantic basin northwards of 30° S and below 500 m, we use ECCO to calculate the observed AMOC strength in the same manner. The RAPID array AMOC strength is inconsistent with this definition since it is fixed at 26.5° N. Note that ECCO tends to underestimate the mean-state AMOC strength implied by the RAPID array at 26.5° N by approximately 1.5 Sv (Extended Data Fig. 3). To account for observational uncertainty in the emergent constraint analysis, we use a Gaussian PDF for the observed AMOC strength. For both datasets, the mean and standard deviation are calculated from the annual-mean time series of the AMOC strength. The AMOC strength from ECCO is calculated over the period 1992–2015 and has a mean and standard deviation of 15.3 Sv and 1.2 Sv, respectively. The AMOC strength from the RAPID array is calculated over the period 2005–2021 and has a mean and standard deviation of 16.7 Sv and 1.4 Sv, respectively.

Thermal-wind expression

The thermal-wind expression (equation (1)) approximates the AMOC strength from the magnitude of the Atlantic basin meridional density difference, $\langle \Delta_y \rho \rangle$, and overturning depth, H, under an assumption of mass conservation between zonal and meridional volume transport[33,37]. The two variables, $\langle \Delta_y \rho \rangle$ and H, are diagnosed from CMIP6 output of ocean potential density in the Atlantic basin[29]. The variable $\langle \Delta_y \rho \rangle$ is calculated as the vertical average of the difference in potential density between the North Atlantic (area-averaged from 40° N to 65° N) and the low-latitude Atlantic (area-averaged from 30° S to 30° N) over the upper 2,000 m of the Atlantic basin. This estimate of $\langle \Delta_y \rho \rangle$ represents the magnitude of the meridional density gradient in the upper cell. The depth H is calculated as the depth where the depth-integrated $\Delta_y \rho$ (for the same regional domains) equals the vertical mean of the depth-integrated $\Delta_y \rho$ (equation (2)). This estimate of H is approximately the depth of maximum zonal volume transport[29] and, assuming weak eastern boundary currents, can be thought of as the depth of maximum meridional volume transport. For the same column-averaged change in $\Delta_y \rho(z)$, a small reduction throughout the entire water column would result in more shoaling of H, whereas a large reduction confined to the surface ocean would lead to less shoaling of H. Note that the results presented in this study do not depend strongly on the exact latitude bounds of the low-latitude Atlantic. This is because the initial AMOC weakening is more strongly controlled by density changes in the North Atlantic. Here the northern region includes the convection region, and the southern region represents interior stratification to the south of the convection region.

Emergent constraint analysis

To obtain a constrained PDF of the change in the AMOC strength $\delta\psi$ for the years 2071–2100, we first calculate a PDF of the observed AMOC strength ψ using ECCO or the RAPID array (see the preceding subsection). We assume the PDF of ψ is Gaussian,

$$P(\psi) = \frac{1}{\sqrt{2\pi\sigma_\psi^2}} \exp\left\{-\frac{(\psi-\bar{\psi})^2}{2\sigma_\psi^2}\right\}, \tag{8}$$

where $\bar{\psi}$ is the mean and σ_ψ is the standard deviation of the observed AMOC strength. We then create a constrained PDF of $\delta\psi$ by combining the PDF of the observed AMOC strength $P(\psi)$ and the PDF of the emergent constraint relationship, which estimates $\delta\psi$ given ψ. The emergent constraint PDF is

$$P\{\delta\psi|\psi\} = \frac{1}{\sqrt{2\pi\sigma_f^2}} \exp\left\{-\frac{(\delta\psi - f(\psi))^2}{2\sigma_f^2}\right\}, \tag{9}$$

where σ_f is the prediction error of the regression and $f(\psi)$ estimates $\delta\psi$ on the basis of ψ (which is described in more detail in the following). Given these two PDFs, $P(\psi)$ and $P\{\delta\psi|\psi\}$, the PDF for $\delta\psi$ is calculated by numerically integrating

$$P(\delta\psi) = \int_{-\infty}^{\infty} P\{\delta\psi|\psi\}\, P(\psi)\, d\psi. \tag{10}$$

In equation (9), $f(\psi)$ is estimated in two separate ways. The first estimate of $f(\psi)$ comes from a linear regression of ψ and $\delta\psi$ based directly on CMIP6 output. This results in

$$f(\psi) = a_\psi + b_\psi \psi, \tag{11}$$

where a_ψ is the intercept and b_ψ is the slope of the linear regression of $\delta\psi$ on ψ. The second estimate of $f(\psi)$ comes from the physical expression introduced in this study, which approximates $\delta\psi$ through equations (5) and (6).

Data availability

We thank the climate modelling groups for producing and making available their model output, which is accessible on the Earth System Grid Federation (ESGF) Portal (https://esgf-node.llnl.gov/search/cmip6/).

Code availability

The code needed to calculate the overturning depth scale is available on Zenodo at https://doi.org/10.5281/zenodo.15103083 (ref. 53).

References

51. McDougall, T. J. & Barker, P. M. Getting started with TEOS-10 and the Gibbs Seawater (GSW) Oceanographic Toolbox. *Scor/Iapso WG* **127**, 1–28 (2011).
52. Marshall, J., Adcroft, A., Hill, C., Perelman, L. & Heisey, C. A finite-volume, incompressible Navier Stokes model for studies of the ocean on parallel computers. *J. Geophys. Res. Oceans* **102**, 5753–5766 (1997).
53. Bonan, D. B. et al. Code & data to accompany "Observational constraints imply limited future Atlantic meridional overturning circulation weakening". *Zenodo* https://doi.org/10.5281/zenodo.15103083 (2025).

Acknowledgements

This work was supported by the National Science Foundation (NSF) Graduate Research Fellowship Program under NSF Award DGE1745301 (D.B.B.), the Cooperative Institute for Climate, Ocean, and Ecosystem Studies (CICOES) under NOAA Cooperative Agreement NA20OAR4320271, Contribution No. 2025-1450 (D.B.B.), the David and Lucile Packard Foundation and NSF Award OCE-1756956 (A.F.T.), Schmidt Sciences, LLC (T.S. and L.Z.), and NSF Awards OCE-1850900 and AGS-1752796 (K.C.A.).

Author contributions

D.B.B. conceived of the project, conducted the analysis, generated the figures and wrote the paper. A.F.T. and T.S. contributed to paper revision and supervised the project. L.Z. and K.C.A. contributed to paper revision and helped interpret results. S.S. contributed to project design and paper revision and helped interpret results.

Competing interests

The authors declare no competing interests.

Additional information

Extended data is available for this paper at https://doi.org/10.1038/s41561-025-01709-0.

Correspondence and requests for materials should be addressed to David B. Bonan.

Peer review information *Nature Geoscience* thanks Wei Cheng and Yen-Ting Hwang and the other, anonymous, reviewer(s) for their contribution to the peer review of this work. Primary Handling Editor: James Super, in collaboration with the *Nature Geoscience* team.

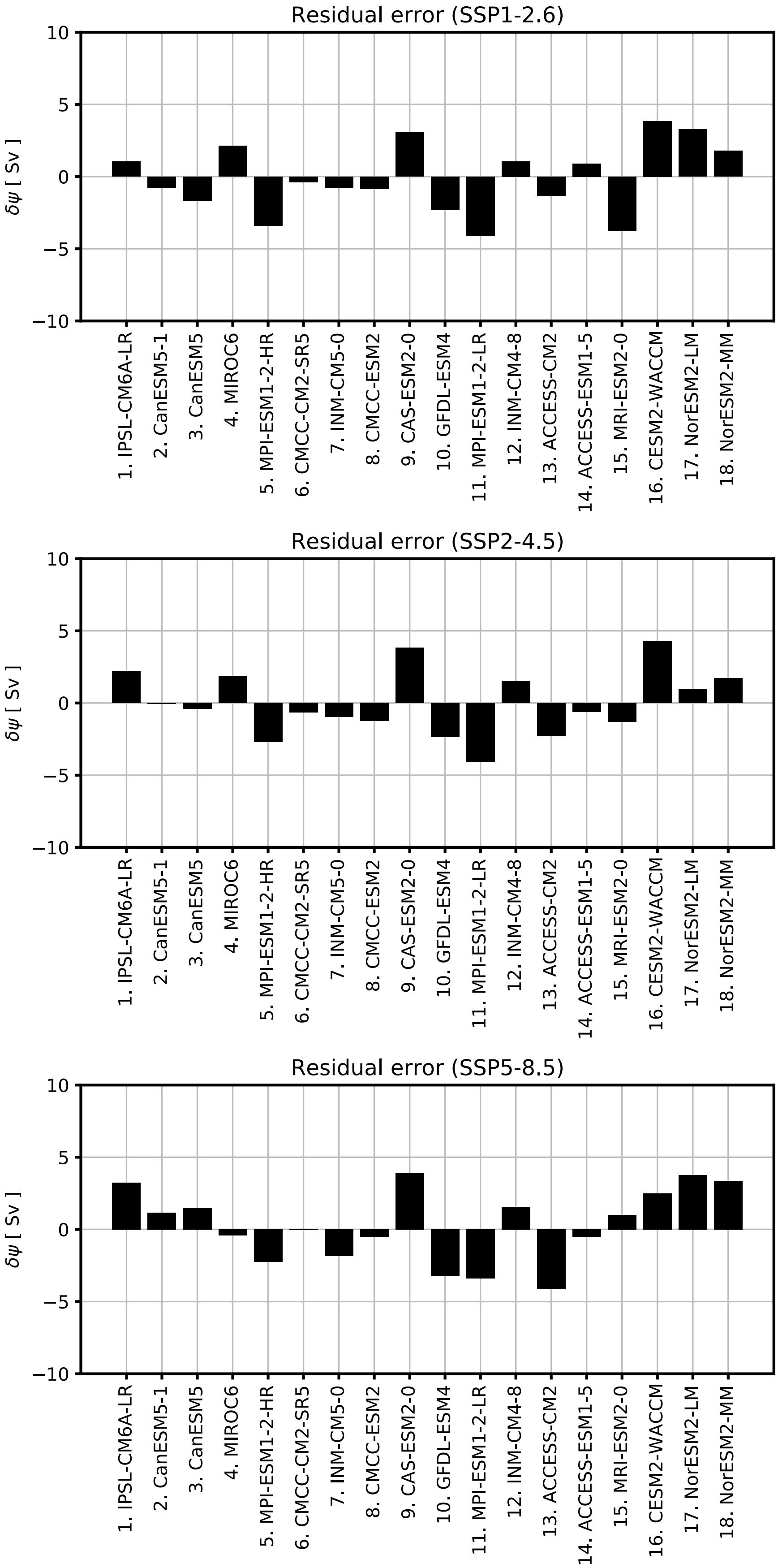

Extended Data Fig. 1 | Comparison of the AMOC weakening calculated in GCMs and predicted by Eq. (3). Bar plots showing the residual error between the AMOC weakening calculated in GCMs and predicted by the thermal- wind expression (Eq. 3) for each emission scenario at years 2071–2100.

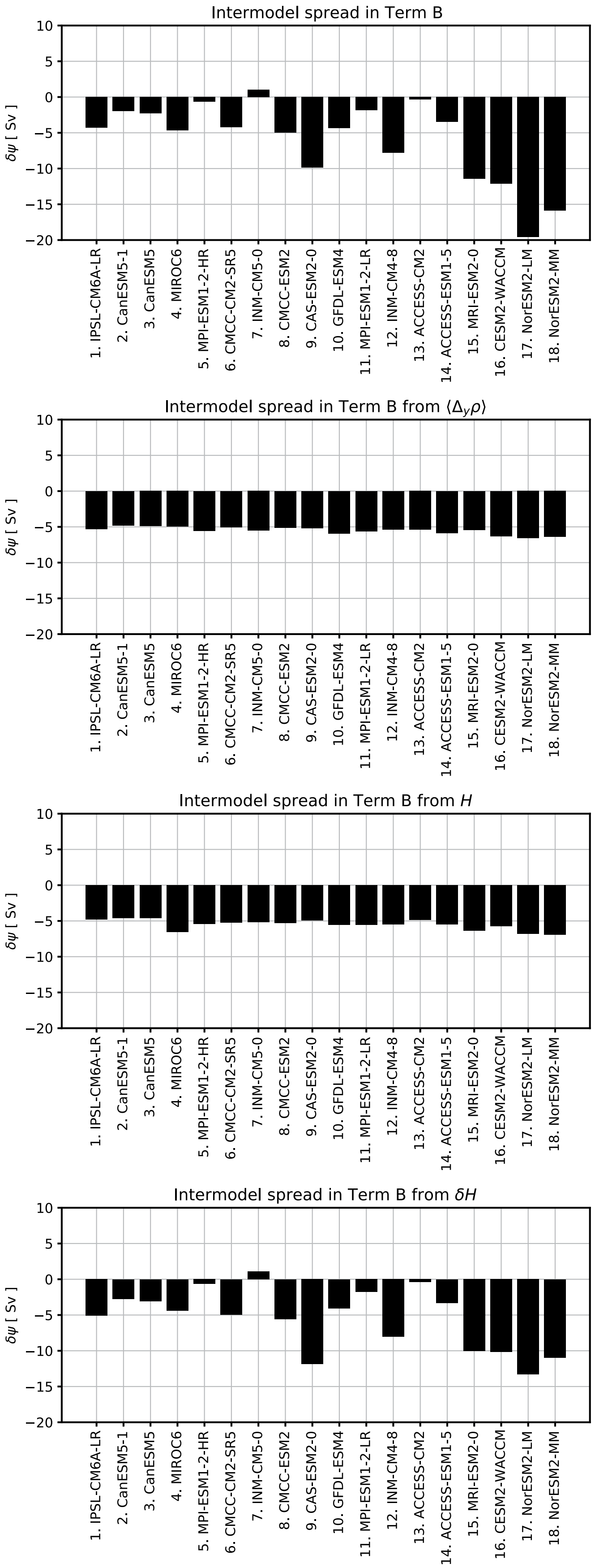

Extended Data Fig. 2 | Contributions of each variable to the intermodel spread in Term B from Eq. (3). The implied AMOC strength change from Term B at years 2071–2100 of the SSP5-8.5 emission scenario. Each panel shows the magnitude of Term B for each GCM when considering the full intermodel spread of all terms ($\langle \Delta_y \rho \rangle$, H, δH) and from H, δH, and ($\langle \Delta_y \rho \rangle$ separately).

https://doi.org/10.1038/s41561-025-01709-0

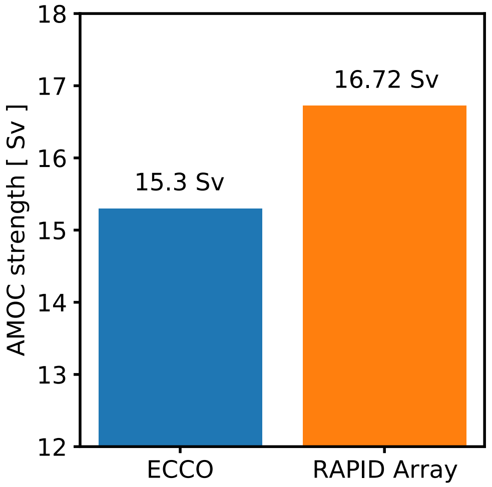

Extended Data Fig. 3 | Observed present-day AMOC strength implied by ECCO and the RAPID array. The present-day annual-mean AMOC strength calculated from ECCO and RAPID array at 26.5°N. The ECCO period is 1992–2017. The RAPID array period is 2005–2021.